3D analysis of dislocation networks in GaN using weak-beam dark-field electron tomography

Jonathan Simon Barnard, Joanne Helen Sharp, Jenna Tong, P A Midgley

3D analysis of dislocation networks in GaN using weak-beam dark-field electron tomography

Journal:	*Philosophical Magazine & Philosophical Magazine Letters*
Manuscript ID:	TPHM-06-Mar-0047.R3
Journal Selection:	Philosophical Magazine
Date Submitted by the Author:	27-Apr-2006
Complete List of Authors:	Barnard, Jonathan; University of Cambridge, Department of Materials Science and Metallurgy Sharp, Joanne; Cambridge University, Department of Materials science and Metallurgy Tong, Jenna; University of Cambridge, Department of Materials Science and Metallurgy Midgley, P; University of Cambridge, Department of Materials Science and Metallurgy
Keywords:	dislocations, GaN, TEM, tomography
Keywords (user supplied):	WBDF

3D analysis of dislocation networks in GaN using weak-beam dark-field electron tomography.

J. S. BARNARD, J. SHARP, J. R. TONG & P. A. MIDGLEY*

Department of Materials Science and Metallurgy,
University of Cambridge,
Pembroke Street,
Cambridge CB2 3QZ, UK.

* Authors for correspondence. E-mail: pam33@cam.ac.uk, jsb43@cam.ac.uk.

Abstract

We have developed a new method of tomographically reconstructing extended three-dimensional dislocation networks using weak-beam dark-field (WBDF) imaging in a TEM. A series of WBDF images is recorded every few degrees over a large tilt range, whilst ensuring that the dark-field reflection used for imaging maintains a constant deviation parameter. With suitable filtering of the WBDF images prior to tomographic reconstruction, the three-dimensional distribution of dislocations is reproduced with high fidelity and high spatial resolution. The success of this approach is demonstrated for heteroepitaxial Mg-doped GaN films. The fidelity of the tomographic reconstruction was found to vary depending on the dislocation line-vector and the elastic anisotropy of the material.

Key words: Dislocation; TEM; WBDF; tomography; GaN

1. Introduction

For fifty years microscopists have studied dislocation networks in the transmission electron microscope (TEM) as essentially two-dimensional projections of a three-dimensional object. Since the first images of dislocations appeared [1], TEM has proved to be pivotal in understanding the importance of dislocations in many materials systems.

It was quickly established that dislocations with Burgers vector, **b**, could be imaged in the TEM using diffracted beam **g** provided that **g**.**b**≠0. The contrast mechanism was first explained in 1960 using kinematic diffraction theory [2] and later using the dynamical theory of Howie and Whelan [3]. The development of the weak-beam dark-field (WBDF) technique by Cockayne *et al* in 1969 [4], enabled dislocations to be imaged with a spatial resolution fine enough to allow individual partial dislocations, separated by ~10 nm, to be distinguished. In the original paper the distance between pairs of Shockley partials in a Cu-Al alloy were measured and used to determine the stacking fault energy.

Progress in the analysis of dislocations continues. Aberration-corrected STEM allows the structure of dislocation cores to be determined with high accuracy [5]. Electron energy loss spectroscopy (EELS) is used to detect chemical segregation at dislocations [6] and determine the electronic state of dislocations through band-gap studies [7]. In addition, electron holography has established the electrostatic potential distribution around charged dislocations as found in optoelectronic materials such as GaN [8].

Here, we demonstrate how the imaging of dislocations can be extended to the third spatial dimension, by combining weak-beam dark-field (WBDF) imaging with electron tomographic reconstructions. As an example, we have been able to reconstruct a three-dimensional dislocation network in a key semiconductor material, GaN, and in so doing correlate the 3D geometry of the network with the growth and plastic deformation of the GaN film.

The image signal used for tomographic reconstruction must satisfy the projection requirement, namely that the signal must be a monotonic function of some physical property. Electron tomography using STEM-HAADF provides quasi-chemical 3D information because, in general, the image intensity scales with atomic

number, Z, as Z^{β} ($1.5<\beta<2.0$) [9] and increases almost linearly with thickness [10]. Likewise, in energy-filtered TEM of relatively thin samples, the image signal is proportional to the elemental concentration and the projected specimen thickness. For example, EFTEM tomography has been successful in reconstructing oxide-shells seen in NiFe nano-particles [10].

In general, diffraction contrast does not satisfy the projection requirement because the bright-field (or dark-field) image intensity varies rapidly and in a complex way with sample orientation and thickness. Dislocations inclined to the electron beam give rise to images with intensity variations that change with crystal orientation. Such complicated intensity variations are not amenable to tomography and so, at first glance, diffraction contrast would appear to be unsuitable for reconstructing objects in three dimensions. In the case of WBDF imaging, the diffraction contrast yields an image of a dislocation which is narrow in width and close to the dislocation core. As will be shown here, the periodic nature of the image contrast does not affect significantly the fidelity of the reconstruction. If the sample is sparsely populated with dislocations, then the degree of overlap between dislocations is small and dislocations should not be difficult to distinguish. Nevertheless, it is important that the WBDF condition is held constant over the entire tilt series, to ensure the dislocation 'image' does not vary in size or position with respect to the core.

As an idea, three-dimensional dislocation imaging is not new. In 1959 Lang developed the topographic x-ray imaging technique to view dislocations in silicon [11] and obtained pseudo-three-dimensional information using stereographic pairs of x-ray topographs taken with $\pm\mathbf{g}$ set to the Bragg condition. Given the large Bragg angles and the fact that, at the Bragg condition, the bulk crystal appears nearly identical (owing to Friedel's law) shifts in the dislocation contrast could be attributed to parallax. This technique, known as stereography, has been used ever since.

The first TEM-based stereographic imaging was used by Basinski to discern the three-dimensionality of dislocation networks in plastically deformed single-crystal copper [12]. Basinski had to rotate the crystal around the Bragg condition to obtain the stereographic perspective (the Bragg angles $\pm\mathbf{g}$ are too small in the TEM), but the effect was essentially the same as Lang's topographic method. TEM stereography uses angles of no more than about 10^{o} (human perception of depth is difficult above this angle), which allows discernment of dislocations at different heights. However,

the actual height *measurement* is altogether more restrictive. Assessments of height differences are usually qualitative unless some prior knowledge is used. For example, Breen was able to distinguish between misfit dislocations in the upper and lower interfaces of a 30nm $In_{0.25}Ga_{0.75}As$-GaAs quantum well using stereometry [13] knowing that misfit dislocations occupied the interfacial planes [14]. Breen also saw that, where orthogonal misfit dislocations crossed in the lower interface, some dislocations bent over into the bulk for short segments at crossing points, owing to dislocation repulsion, but was unable to measure how deep this occurred. To do so, Breen would have needed a method with better depth resolution and this requires genuine three-dimensional imaging.

It was not until 2001 that full three-dimensional reconstructions of dislocations were obtained by x-ray topographic imaging using a synchrotron source [15]. Dislocations in millimetre-sized pieces of synthetic diamond were reconstructed using a tilt series of Lang-topographs, a technique called "topo-tomography", over a 360^{o} tilt range. The width of the contrast associated with x-ray topographic images of dislocations is ~1μm and so the technique is limited to imaging dislocations spaced more than a few microns apart, giving a practical density limit of about 10^{6} dislocations cm^{-2} for dislocations imaged this way.

Dislocation tomography for materials systems with much higher dislocation densities therefore requires a new approach. As Hirsch *et al* first showed fifty years ago, it is an approach for which the TEM is perfectly equipped.

2. Materials

To test the weak-beam tomography method, we studied a heteroepitaxial gallium nitride film, grown on c-plane sapphire (α-Al_2O_3) with a high dislocation density. The lattice mismatch of this system is large (~14%); without a nucleation layer rough, three-dimensional films are grown; with a nucleation layer, planar films can be achieved [16]. In this case, most of the misfit is taken up by a nucleation layer, which is a 30-50nm thick dislocation-rich layer immediately adjacent to the sapphire (Figure 1). High-resolution lattice images of the nucleation layer showed the layer contained a high density of stacking faults and dislocations, a fraction of which propagate into the film. The result is a flat GaN film with a threading dislocation density of 10^{9} to 10^{10} cm^{-2}. The dislocation line vector, **u**, is almost always parallel to [0001] and the

Burgers vector, **b**, is almost invariably either **a**-type (threading-edge) or **a+c**-type (threading-mixed). Fewer than 1% of the dislocations in these samples were **c**-type (threading-screw).

[Insert figure 1 about here]

The GaN films were doped with magnesium to make them p-type. Magnesium doping of GaN is fraught with difficulties, notably that the magnesium forms a very deep acceptor level (~200meV) and has an affinity to hydrogen that results in the formation of a Mg-H defect complex [17]. These phenomena combine to make defect-free Mg-doped GaN difficult to grow. The high donor energy requires a high Mg concentration to achieve a modest hole concentration; only 1% of Mg atoms are ionised at room temperature and it is not unusual to have magnesium concentrations greater than 10^{20} cm^{-3} to achieve significant hole concentrations. However, the strain associated with the formation of the Mg-H defect complex ensures that the Mg-doped GaN layer is compressively strained if grown onto unstrained GaN [18]. Since the Mg-H complex is electrically inactive, it has to be dissociated to enable hole conduction. The earliest improvements in hole conduction were achieved with low-energy electron beam irradiation (LEEBI) in the SEM with beam energies of about 10keV [19]. It was later established that electron beam heating improved the electrical properties of the film and so rapid thermal annealing (RTA) supplanted the LEEBI method as a way to achieve device-grade p-GaN. Optimal RTA is now performed at temperatures between 800 and 900^{o}C for a short period of time [17].

The sample we studied here is a 1.5 μm-thick Mg-doped GaN film grown on 3μm of undoped GaN, which is grown on sapphire by metal organic vapour-phase epitaxy (MOVPE). The sample was one of a batch in which the partial pressures of the magnesium and gallium precursor gases (bis-cyclopentadiethyl magnesium and tri-methyl gallium) were varied to test the growth conditions. After growth, samples were split into two prior to electrical testing; one half of the set was RTA-treated, while the other was not.

Photoluminescence spectra of these samples showed the significant intensity within a broad yellow peak below the direct-gap emission energy [20]. The yellow band is attributed to the deep defect level created by the magnesium. Secondary ion

mass spectrometry (SIMS) showed that the magnesium concentration was not constant throughout the intended volume. The first 600nm of the Mg-doped GaN grown had a Mg concentration of ~6×10^{16} cm^{-3}, but then rose to a concentration of ~5×10^{18} cm^{-3} in the uppermost 900nm [20]. Such delayed incorporation of magnesium is not uncommon.

TEM-based comparisons of the RTA and non-RTA treated films showed very similar microstructure suggesting that plastic relaxation had occurred during the growth of the Mg-doped GaN. Both showed the presence of near-surface cracking resulting in partial delamination of the GaN film. The tips of these delaminating cracks were always seen close to bands of dislocation half-loops aligned along the <1-100> directions (Figure 2). Around the crack body were large numbers of in-plane dislocation loops that bowed out of the highly deformed region (Figure 3). Dark-field images taken with the set of {1-100} reflections showed that the curved in-plane dislocations all had the same Burgers vector, 1/3[11-20], (Figure 3) and extended no more than a few microns. Careful examination showed that these loops were pinned at threading dislocations in the film. Several linear dislocations were also seen to extended along the [2-1-10] and [-12-10] directions in figure 3(c), but their Burgers vectors are difficult to ascertain. For example, the right-hand dislocation extending out to the upper right seems to disappear in the (-1010) reflection but not the (01-10), suggesting a Burgers vector of 1/3[-12-10]. However, given the strong contrast of the loops in these reflections, it is difficult to be certain.

[Insert figures 2 and 3 about here]

Figure 4 shows dark-field large-angle convergent beam electron diffraction (LACBED) patterns, recorded using the reflection **g**=(11-20), that were used to measure the total strain of the GaN around the crack tip and body. Starting at the tip, where the dislocation bands were seen (Figure 2), the lattice rotation is modest. Some buckling of the film is evident from the curvature of the dark-field rocking curves (Figure 4(a)), but the displacement of the rocking curve is small across the dislocation bundles. The dark-field rocking curve was seen to split as it was moved into the crack body (Figure 4(b)) indicating a twist in the crystal in passing either side of the crack. Well into the cracks, large changes (~50mrad) in the crystal orientation could be seen

(Figure 4(c)). Such angles could be accounted for by arrays of **a**-type dislocations with an average spacing of ~60Å. The fact that these cracks were found in thin plan-view specimens, testified to the near-surface nature of the plastic relaxation mechanism i.e. the delamination did *not* appear to coincide with the Mg:GaN/GaN interface.

[Insert figure 4 about here]

3. Method

Successful tomography requires that each projection in the tilt series suffers no resolution loss over the area of interest. It is worth pointing out that the imaging properties of WBDF imaging were sympathetic to this, provided that the area of interest is not too extensive. The spatial resolution, d_R, of a WBDF image diffraction-limited by the objective aperture (diameter 2β), and is given by the Rayleigh limit

$$d_R = 0.6\frac{\lambda}{\beta} \qquad (1)$$

For a 300keV electron beam and an objective aperture of β=1mrad, the resolution, d_R, is 1.2nm. The depth of field, Δ, over which this resolution is maintained is given by the following

$$\Delta = \frac{d_R}{\beta} \qquad (2)$$

and so, for nanometre resolution throughout the series, the projected thickness of the sample must not be greater than ~1000nm. This imposes a limit on the lateral extension, l_{max}, that can be tomographically reconstructed for given resolution and maximum tilt angle, θ_{max}. Ignoring the thickness of the specimen, this lateral limit is therefore

$$l_{\max} = \frac{\Delta}{\sin\theta_{\max}} = \frac{d_R}{\beta\sin\theta_{\max}} \qquad (3)$$

thus restricting our reconstructed field of view to a width of about 1.4μm, for a maximum tilt of 60°.

For the purpose of maintaining a constant deviation parameter, the tilt-axis of the holder must lie parallel (or anti-parallel) to the direction of the reciprocal lattice

vector used for imaging. To this effect, the sample must either be sympathetically mounted on a single-axis holder, or, by using a tilt-rotate holder and finding a suitable condition *ad hoc*; we chose the latter. To achieve high tilts within the pole-piece gap of the microscope used here, a Philips CM30 TEM with a SuperTWIN lens, required machining away any excess material on a standard Philips tilt-rotate holder. A reduction in holder width from 6.0mm to 5.1mm, allowed a tilt range of ±60^{o} to be used in the tilt-series seen here.

The hexagonal symmetry of GaN has one particular advantage with regard to dislocation imaging in a dark-field reflection. The primary visibility condition for imaging a dislocation is $\mathbf{g}.\mathbf{b}\neq 0$ (for edge dislocations with $\mathbf{g}.\mathbf{b}=0$, a secondary condition of $\mathbf{g}.\mathbf{b}\wedge\mathbf{u}\neq 0$ gives weaker dislocation contrast) [21]. It is found that, for a dark-field image taken with any of the {11-20} reflections, the condition $\mathbf{g}.\mathbf{b}\neq 0$ holds for all dislocations with an **a** component. Plan-view GaN specimens viewed along the <0001> direction have three sets of intersecting {11-20} Kikuchi lines which improved the likelihood of achieving the correct geometry for a WBDF tilt-series. For the tilt series acquired here, we imaged using the (11-20) reflection while keeping the Bragg condition between the (33-60) and the (44-80) reflections.

A magnification of 9000× was used throughout the series and all the lenses were held at constant excitation to prevent small image rotations between images. The specimen was refocused using the eucentric height control. The tilt series comprised of 25 images, covering a 120^{o} tilt range and recorded in 5^{o} increments on standard negatives. Each negative was digitised using a high-resolution scanner with a sampling rate of 1200dpi (1.2nm/pixel). To enhance the dislocation contrast the images were filtered to remove low spatial frequency intensity variations associated with broad bend contours. This entailed subtracting a highly smoothed version of the image from its original to enhance the high-spatial frequencies. Fourier-based filtering was found not to work because of the introduction of unwanted artefacts in the filtered images. The three-dimensional reconstruction was performed using weighted back-projection (WBP) and sequentially iterated reconstruction technique (SIRT) routines written in the programming language IDL (Research Systems Inc.). The SIRT routine was found to give optimum reconstructions when run with 10 iterations per slice; the reconstruction of 512^{3} voxels corresponded to an object volume of (1200nm)^{3}.

4. Tilt-series acquisition

The experimental set-up used for the WBDF tilt series had to meet several criteria to yield a good reconstruction. First, we had to make sure that the Bragg condition remained constant throughout the tilt range. Thin-film relaxation made this difficult for areas containing either cracks or dense dislocation bundles. A compromise was found in those areas immediately adjacent to the crack tip (Figure 4). The lattice rotation of the GaN around the crack body was very large, (~40-50 mrads) as seen in the (11-20) dark-field LACBED patterns of figure 4. Imaging dislocations either side of the crack simultaneously in a single tilt series was therefore problematic. Second, the visibility of the dislocations in each image of the tilt-series had to be sufficiently high for successful image processing. In this case, an energy filter was not available and inelastic scattering can become significant at high tilts; at 60^{o} for a slab-like specimen its projected thickness is twice that at zero tilt. Near the <0001> zone axis the images of the threading dislocations become very short, making alignment of successive images difficult. In-plane dislocations were found to be essential for alignment of images close to normal incidence.

[Insert figure 5 about here]

The area imaged was immediately adjacent to a dislocation bundle associated with a crack-tip (Figure 5). Across the field of view we were able to maintain a $\mathbf{g}(3.6\pm0.5\mathbf{g})$ WBDF diffraction condition with $\mathbf{g}=\{11\text{-}20\}$ and $s_g = 1.0\pm0.2\times10^{-2}$ Å^{-1} where, throughout the tilt-range, the dark-field reflection remained approximately parallel to the optic axis of the microscope. Selected area diffraction patterns recorded at either end of the tilt series showed that this condition varied little over the tilt series

5. Image Processing and Reconstruction

Each WBDF image in the series was scanned into a computer but no attempt was made to make the intensities truly quantitative. The images were processed in IDL to remove the strong variations in intensity associated with broad bend contours and changes in the bulk intensity owing to the changing diffraction conditions. This

filtering involved smoothing the images using a 7×7 pixel kernel and repeating the process five or six times. The intensity associated with the dislocations dissipates rapidly into the background, so that, when the smoothed image is subtracted, the high-spatial frequency components remain. These images were then assembled into a three-dimensional stack and aligned using cross-correlation algorithms, taking into account the differences in tilt, i.e. stretching or compressing the image to compensate between successive tilts. Each image is aligned to a common centre coincident with the tilt axis. Prior to reconstruction, the orientation of the tilt axis is established by examining the quality of back-projections taken from several slices along the proposed axis. If the axis is mis-orientated, then features in the reconstructed slices are smeared into arcs, with the slice at either end having an opposite sense of arcing [22]. Once the parameters of the axis are found, the data is processed with the SIRT algorithm that minimises differences between the experimental data and *reprojections* of the trial reconstruction. SIRT does this slice-by-slice along the entire axis. SIRT returns a cubic volume with a linear extension identical to the input image size, in this case 512×512 pixels.

A voxel-projection of the reconstruction can be seen in figure 6 with a viewing angle corresponding to a 45^{o} sample tilt[1]. The volume of material seen here is 1200×1200×300nm^{3}. Near the sample edge, the reconstruction looks 'dusty' and, whilst threading dislocations can be seen, they are difficult to distinguish. The 'dust' arises from residual contrast related to the intense thickness fringes seen close to the edge. The only object within a reconstruction consistent with these fringes is one that extends throughout the whole reconstruction volume, beyond the surface of the sample. With the reconstruction deliberately truncated to exclude the regions corresponding to vacuum above and below the specimen, the effect is a residual 'dusty' object that pervades the entire reconstruction.

[Insert figure 6 about here]

The threading dislocation contrast near the edge shows a characteristic drop in intensity as the dislocation approaches the bottom surface. Strong contrast could be seen at the end of the threading dislocations on one side only of the filtered images

[1] See also accompanying movie

(Figure 5(b)). In the reconstructed volume, the images of these dislocations tended to be thick and intense at one end and diffuse and weak at the other (**A** in figure 6). Indeed, when viewed edge-on (corresponding to a sample tilt of 90^{o}) the upper ends of the dislocations delineated the upper surface quite clearly, while the bottom surface is hardly distinguishable. These threading dislocations also show periodic intensity variations when viewed at certain angles, attributable to strong dynamical diffraction contrast at certain crystal orientations. For example, low-angle domain boundaries bounded by edge dislocations rotate the interior of the domain towards the Bragg condition for a near-excited reflection (**A** in figure 5(a)). The result is a bright region with periodic contrast towards one end of the dislocation. In the filtered image the asymmetry in dislocation contrast is more evident (**A** in figure 5(b)).

[Insert figure 7 about here]

The reconstruction in the thicker part of the specimen has an altogether different appearance. Here, the threading dislocations do not show such strong dynamical thickness variations and the contrast is reasonably constant. The threading dislocations in this region do not show the strong intensity oscillations seen in the thinner regions and the degree of intensity asymmetry is reduced. The in-plane dislocations (**B**) show near-constant visibility in the tilt series, resulting in the strong registry in the reconstruction. In particular, the reconstruction is of sufficient fidelity to show clearly that the dislocations turn over at various heights within the film and glide away from the crack-tip dislocation bundle. This can be seen much more clearly when the thin regions have been removed and the in-plane segments viewed without obstruction (Figure 7). Investigation of these dislocations showed that they are pure edge dislocations that turn over to become pure screw type. In figure 7(a) we see that two threading edge dislocations turn over within the crack-tip dislocation bundle and glide away to the left leaving a screw segment behind (**B**). One of these dislocations interacts directly with another threading dislocation (**D** in figure 7), forcing the in-plane screw dislocation to turn upwards (becoming mixed) before resuming its glide away from the crack-tip region. Another dislocation (**E**) towards the front of figure 6 appears to have changed its habit plane briefly around 50nm from the edge of the reconstruction, before resuming its previous glide direction (**E** in figure 7). The reverse view of this region, figure 7(b), shows that the glide-planes of these

dislocations are distinctly different. The crack-tip dislocation bundle lies to the left of the image (**C**) and we see that the in-plane screw dislocations (**B**) are seen to form by threading dislocations that turn over within the crack-tip dislocation bundle. The interaction of the in-plane dislocation with a threading dislocation is seen more clearly in this view too (**D**). In particular the threading dislocation line vector is slightly tilted from the <0001> axis and the in-plane segment towards the right of the threading dislocation in figure 6 is very clearly reconstructed (upper left of **D** in figure 6).

Figure 6 strengthens our assertion that in-plane screw segments are formed by the glide of threading edge dislocations. On the right-hand side of this figure an in-plane dislocation is seen to glide *into* the volume of interest and terminate on the upper surface. This dislocation does not terminate at right angles to the film, but at a slight angle, indicating that a shear stress exists that pushes against this dislocation. Equilibrium is maintained by the friction stress associated with moving the dislocation.

Dislocations in the crack-tip bundle were not resolved using the WBDF tomography technique. The dislocation spacing within this region was <10nm, establishing a practical limit of the method for dislocation densities of ~10^{12} cm^{-2}. The diffuse contrast associated with the crack-tip dislocation bundle in figures 7(a) and (b) suggests that the bundle sits about 200nm below the upper surface. This is below the height at which local threading dislocations turn over to become in-plane screws.

One feature common to all the in-plane dislocations seen in the reconstruction is the elongation of the dislocation contrast along the vertical direction. The effect is to broaden the dislocation line into a thin 'lath'. The limited range of tilt in the series may account for this. Missing spatial frequencies along the vertical directions (the so called 'missing wedge') conspire to extend the object along that direction. This elongation factor, e, is related to the maximum tilt angle, θ_{max}, in the tilt-series by

$$e = \sqrt{\frac{\theta_{\max} + \sin\theta_{\max}\cos\theta_{\max}}{\theta_{\max} - \sin\theta_{\max}\cos\theta_{\max}}} \qquad (4)$$

where θ_{max} is expressed in radians. For the series discussed here, the elongation factor is 1.5. However, this factor appears to underestimate the elongation seen in the reconstruction. Figure 7(b) shows that the dislocation width is about 20nm along the

<0001> direction, but only 10nm in the lateral direction, an elongation factor twice that given by equation (4). However, cross-sections of the dislocations (figure 8) show that the actual intensity distribution is sharper. For the group of three in-plane dislocations that glide out of the cracked area (**D1**, **D2** and **D3**), the width of the dislocations is about ~5nm while they stand about ~10nm high. The in-gliding dislocation (**F**) has an altogether different appearance. This dislocation is strongly arced with an arc-length of about 20-40nm with a width of ~5-10nm.

6. Discussion

In contrast to the relatively easy applicability of stereographic methods, WBDF tomography requires a demanding experimental configuration (to maintain the constant diffraction condition) and exposes the sample to a high electron dose- so what are the advantages of an electron tomography approach?

The primary advantage is the *precision* to which the dislocation position can be recovered. Figure 9 demonstrates the advantage of the method for a simple test object (figure 9(a)), in this case three dislocations at different heights in a film that are reconstructed stereographically (figure 9(b)) and tomographically (figure 9(c)). The error in the stereo-pair is determined by the width of the dislocation contrast, *w*, and the stereo-angle (θ_S) to be: $w/\sin(\theta_S)$. For a contrast width of 2nm, we find the stereometric error to be ~20nm, which is too high to be able to determine whether the dislocations are genuinely separated in height. With the simple back-projection of the tomographic series ($\pm 60^o$) we find the contrast width is smaller, ~5nm, which is fine enough to determine the relative heights of the dislocations. With the SIRT algorithms we are able to remove the 'fans' associated with the back-projection and this appears to improve the effective depth-resolution to about 3nm. Such resolution would be advantageous where dislocations are seen in poorly defined hetero-interfaces such as those due to compositional grading or interfacial diffusion [23].

A secondary advantage of tomographic reconstruction is the ability view the dislocation array from any angle. Our ability to isolate and view dislocation interactions in the plane of the sample affords us new perspectives. For example, in figure 7, we can say with confidence that two dislocations coincide within a volume of only a few nanometers.

That the fidelity of the reconstructed dislocations varies according to dislocation type should not be a surprise. The most obvious improvement to the reconstruction would be the elimination of thickness fringes associated with tapered specimen edges. Improvements in sample preparation techniques may circumvent this; for example, using a focused ion beam (FIB) workstation allows the preparation of flat parallel-sided slabs and mechanical polishing systems based on the tripod-polisher concept allows for wedge shaped specimens with planar surfaces. Thickness fringes for a perfect wedge would be periodic and could be removed relatively easily with a suitable Fourier filter.

In addition to thickness fringes, inelastic scattering and anomalous absorption in the dark-field image were serious obstacles to high-fidelity reconstructions of threading dislocations. Anomalous absorption results in significant differences in the dislocation visibility at the top and bottom surfaces. Such effects are well known [21] and can be minimized for specimens with low atomic number and with the use of higher beam energies. Zero-loss filtering using an in-column or post-column energy filter would improve dislocation visibility considerably, particularly in the thicker regions of the sample.

In contrast to the relatively poor reconstruction of the threading dislocations, the in-plane dislocations were highly visible in the reconstruction, attributable to their near-constant intensity throughout the tilt-series. The use of the in-plane dislocations to align the WBDF images at near-zero-tilt angles helped improve the overall reconstruction of some dislocations, but not others (figure 8). Arcing of such dislocations suggests that the *relative* positions of the WBDF image peaks moved during the series acquisition. Possible sources of motion include elastic anisotropy, changes in the diffraction condition and changes in the projected thickness with tilt-angle. We now examine the influence of each of these in turn, assuming that each image in the tilt-series is aligned perfectly.

The dislocation intensity in a WBDF image is dominated by elastic scattering close to the dislocation core. This occurs because the twist in the lattice rotates the crystal into the Bragg condition locally so that the effective deviation parameter, s_{eff}, tends to zero on one side of the core [24]. Using this stationary point approach leads to the following condition for predicting the vector, $\boldsymbol{r}_0$, that connects the dislocation core to the position of the intensity maximum

$$s_{eff} \approx s_g + \mathbf{g} \cdot \left. \frac{d\mathbf{R}}{dz} \right|_{\mathbf{r}_0} = 0 \quad (5)$$

where z describes the direction of the electron beam and $\boldsymbol{R}$ is the displacement field around the dislocation. If the displacement field is known, the position of the stationary point $\boldsymbol{r}_0$ can be found. The in-plane screw dislocation lies on the basal plane and is coincident with the rotation axis. In a hexagonal material, the distance between the stationary point and the dislocation core changes with the angle, θ, between the electron beam and the **c**-axis of the sample [25, 26]. The core-peak distance, $\boldsymbol{r}_0(\theta)$, becomes

$$r_0(\theta) = \frac{\mathbf{g} \cdot \mathbf{b}}{2\pi s_g^{eff}} \frac{\sqrt{c_{66}/c_{44}}}{\left(1 + \left(\frac{c_{66}}{c_{44}} - 1\right)\sin^2\theta\right)} \quad (6)$$

where the coefficients c_{44} and c_{66} are elastic stiffness constants. The locus of this equation for a fixed effective deviation parameter is an ellipse with a semi-major axis of length

$$r_0^{max} = r_0(0^o) = \frac{\mathbf{g.b}}{2\pi s_{eff}^g} \sqrt{\frac{c_{66}}{c_{44}}} \quad (7)$$

and a semi-minor axis of

$$r_0^{min} = r_0(90^o) = \frac{\mathbf{g.b}}{2\pi s_{eff}^g} \sqrt{\frac{c_{44}}{c_{66}}} \quad (8)$$

[Insert figure 10 about here]

For GaN the elastic constants are c_{44}=24 GPa and c_{66}=83 GPa [27], suggesting an ellipsoid with an aspect ratio of 3.5 that is elongated in the basal plane (Figure 10(b)). For the limited tilt range used here (±60°), the two extremes of core-to-peak distance are found to be: 1.2nm (θ=60°) and 3.8nm (θ=0°), suggesting that the reconstruction image of the dislocation viewed end-on should be composed of an arc that is symmetric about the horizontal (figure 10(c)). For a Burgers vector of opposite sign, the arcing would be reversed relative to the core.

The diffraction condition will vary if the rotation axis of the sample is not exactly parallel to the diffracted beam of interest. The manifestation of such an error is the sinusoidal motion of the WBDF peak relative to the dislocation core as we

proceed through the tilt-series. The extremes in deviation of the WBDF peak would then occur at tilt angles of ±90°, so that the reconstruction image becomes elliptical and asymmetric with respect to the core (figure 10(d)). For a finite tilt-range, we recover an arc of limited length with a ratio of the minimum to maximum distances between the WBDF peaks given by

$$\frac{r_0(+\theta_{\max})}{r_0(-\theta_{\max})} = \frac{s_{eff}^{g,\min}}{s_{eff}^{g,\max}} \qquad (9)$$

Thus, given the deviation parameter and its error ($\mathbf{s_g}$=1.0±0.2×10^{-2}Å), we estimate this variation to be about 0.76 or about 3:4. Its appearance in the reconstruction would thus be an arc that is slightly 'twisted' i.e. the top end would be further away from the dislocation than the bottom, but the extent of this twist would be only about 30%.

The variation of the WBDF peak with projected sample thickness is harder to predict. The peak position does move with specimen thickness in a complicated manner [21]. However this motion would, like the elastic anisotropy, be symmetrical with sample tilt and it is expected that the arcing described in figure 10 would be similar for changes in projected thickness. Couple this with the fact that each dislocation is at a different distance from the entrance surface of the sample, and we see that the appearance of each dislocation will thus depend on the sample tilt in a slightly different way.

Views of the three in-plane dislocations along their line vector (figure 8, **D1-3**), do not show much evidence for the elliptical structure predicted in figure 10. The prevention of the elliptical shape may occur during the alignment process, which automatically suppresses lateral misalignment. This may account for the in-plane segment that glides into the field of view (Figure 6 & 8, **F**). The reconstructed contrast associated with this dislocation is confined to a thin band and suggests that this dislocation may have split into a pair of partial dislocations and a stacking fault. This is not unreasonable, but the separations suggested here should have given stacking fault contrast in images taken in our original analysis of the area (we examined a number of dark-field images prior to acquisition of the tilt series), and this was not seen. To improve the tilt-series alignment, we relied on the three in-plane segments that leave the vicinity of the cracked area towards the right (**D1-3**, figure 6). The

similar glide behaviour of the three dislocations suggests identical Burgers vectors and hence similar core-peak distance profiles in the tomographic series. If arcing is suppressed for these three dislocations, the consequences for the dislocation that glides *in*, is an exacerbation of the arcing effect, *if* the Burgers vector is opposite to the other three in-plane dislocations. Either way, the reliance on in-plane dislocations with high-visibility contrast at low sample tilt-angles may inadvertently lead to the misalignment of other dislocations with different Burgers vectors.

Compared to the possible artefacts shown in figure 10, the extent and symmetry of the arcing observed for dislocation **F** in figure 8 suggests tilt-axis misalignment. The severity of this asymmetry suggests either that this misalignment is large or that our analysis of the artefacts above is overly simplistic. In particular, the actual depth dependence of the dislocation contrast and it variation with projected thickness remains unknown at this stage. To answer this question, we are currently working on the reconstruction of *simulated* images of dislocations, for which the misalignment, along with all the other parameters ($\mathbf{s_g}$, thickness, tilt asymmetry, etc.) can be factored in case by case.

[Insert figure 11 about here]

The microstructure of this sample is both fascinating and complicated and it is worth commenting on what we have learnt from the tomographic reconstructions as well as the microstructural characterisation presented herewith (we refer to figure 11 which presents schematically the essential features of the microstructure seen). It is surprising that the p-type layer appears to degrade in the near-surface region: Matthews and Blakeslee showed that the relief of lattice misfit by dislocation turn-over and in-plane propagation is energetically most favourable at the interface where the shear stress is greatest [14, 23]. However, the fact that delamination occurs so far away from the Mg:GaN/GaN interface leads one to believe that crack formation occurs due to defect formation at or near the surface.

The increase in the number of dislocation half-loops towards the crack tip (Figure 2; **1** in figure 11), leads one to believe that the crack tip occurs by the coincidence of several dislocations with the same Burgers vector on the same slip-plane. Such dislocation formation has been seen to occur in compressively stressed InGaN/GaN films, where the threading dislocation density is very low [28]. Here,

Srinivasan *et al* showed that the dislocation slip system with the greatest net force, taking into account misfit stress, dislocation line tension and Peierls force, had a Burgers vector of 1/3<11-23> on a {11-22} slip-plane. These loops were then seen to cross-slip onto the basal plane coincident with the InGaN/GaN surface and thereafter propagate along the <1-100> directions. However, the conditions for such 1/3<11-23> dislocation formation were different to the case here. Their films had threading dislocation densities of ~10^6 cm^{-2}, some three orders of magnitude smaller than ours. However, this slip system may be easier to nucleate if the GaN film is doped with magnesium. Explanations as to how Mg doping may affect the plasticity of the film vary. The high incidence of yellow luminescence seen from the Mg-doped films suggests that, at the growth temperature, the Mg-doped GaN absorbs more radiation than the undoped GaN underneath. This is the radiation-enhanced dislocation glide effect or photoplastic effect [29], but this seems unlikely given that we have not seen any motion of dislocations under the electron beam, equivalent to extremely high photon flux [30]. A more convincing explanation is that the magnesium in the film enhances the nucleation and subsequent glide of <11-23>/3 dislocations. The motion of dislocations is influenced by electronic effects [29] and may be affected by either the Mg acceptor or the hydrogen released from the Mg-H defect. Enhanced dislocation glide was seen in films of Si, Ge and GaAs exposed to hydrogen plasmas. Arrhenius analysis of the dislocation glide behaviour showed a distinct lowering of the glide activation energy [31]. This is not unreasonable given that, during the RTA treatment, threading dislocations in the vicinity of the crack turn over and glide (**3** in figure 11). The electron tomographic reconstruction of such dislocations has confirmed their origin. The rest of the microstructure, such as the dislocation loops that form at the edge of the crack body seen in figure 3 (**4** in figure 11), seem to come about as a consequence of the delaminating crack. Their limited extension into the film suggests their glide motion is severely hampered, either by pinning at threading dislocations (figure 3) or high glide activation energies.

So far we have only speculated on the role of the dislocation bundles, formed by the half-loops seen in figure 3 (**1** in figure 11), on the formation of the delaminating crack. Our next aim is to develop the dislocation tomography method to allow the resolution of dislocations within the bundles that precede the crack tip. For this we have developed improved filters that allow better isolation of the WBDF intensity maxima. Such filters do return very fine dislocation-related contrast, and this

requires unprecedented levels of precision when aligning the images. These filters are based on line-finding algorithms that examine the curvature of the intensity in the image along certain directions and look at how this correlates from point to point [32].

From a materials perspective we are looking to explore WBDF tomography in several other systems. One such example is the γ-γ' Ni superalloy system, where creep occurs through the motion of misfit dislocations in the γ matrix.

7. Conclusion

We have shown that weak-beam dark-field imaging combined with electron tomography allows the reconstruction of dislocations with high fidelity. The fidelity does vary with dislocation type and we have suggested that the appearance of tomographically reconstructed dislocations is dependent on both the tilt-axis misalignment and material anisotropy. By applying WBDF electron tomography to p-type GaN films we have shown that threading-edge dislocations are able to turn over and glide during RTA annealing leaving an in-plane screw segment.

8. Acknowledgements

We acknowledge Dr Menno Kappers and Prof. Colin Humphreys for the provision of the GaN sample. JS acknowledges Newnham College, Cambridge for financial support.

References

[1] P. B. Hirsch, R. W. Horne and M. J. Whelan, Phil. Mag. **1** 677 (1956)

[2] P. B. Hirsch, A. Howie and M. J. Whelan, Phil. Trans. Roy. Soc. **A252** 499 (1960)

[3] A. Howie and M. J. Whelan, Proc. Roy. Soc. **A267** 206 (1962)

[4] D. J. H. Cockayne, I. L. F. Ray and M. J. Whelan, Phil. Mag. **20** 1265 (1969)

[5] I. Arslan, A. Bleloch, E. A. Stach, and N. D. Browning, Phys. Rev. Lett.**94** 025504 (2005)

[6] M. Hawkridge and D. Cherns, Appl. Phys. Lett. **87** 221903 (2005)

[7] P. E. Batson, K. L. Kavanagh, J. M. Woodall and J. W. Mayer, Phys. Rev. Lett **57** 2729 (1986)

[8] D. Cherns and C. G. Jiao, Phys. Rev. Lett. **87** 205504 2001

[9] E. J. Kirkland, *Advanced Computing in Electron Microscopy* (Plenum, New York, 1998)

[10] M. Weyland and P. A. Midgley, Materials Today **7**(12) 32 (2005)

[11] A. R. Lang, Acta. Cryst. **12** 249 (1959)

[12] Z. S. Basinski, Proc. 5th ICEM B13 (1962)

[13] K. R. Breen, Jnl. Elec. Mat. **21** 409 (1992)

[14] J. W. Matthews and A. E. Blakeslee, J. Crys. Growth **27** 118 (1974)

[15] W. Ludwig, P. Cloetens, J. Härtwig, B. Hamelin and P. Bastie, J. Appl. Cryst. **34** 602 (2001)

[16] H. Amano, M. Kito, K. Hiramatsu and I. Akasaki, Jap. Jnl. Appl. Phys. **28** L2112 (1989)

[17] S. Nakamura, N. Iwasa, M. Senoh, and T. Mukai, Jpn. Jnl. Appl. Phys. **31** (9A) 2883 (1992)

[18] O. Briot, in *Group III Nitride Semiconductor Compounds*, chapter 3 pp70-122 (Clarendon Press, Oxford, U.K., 1997)

[19] H. Amano, N. Sawaki, I. Akasaki and Y. Toyoda, Appl. Phys. Lett. **48** 353 (1986)

[20] M. J. Kappers, Private communication 2001

[21] P. B. Hirsch, A. Howie, R. Nicholson, D. W. Pashley and M. J. Whelan, *Electron Microscopy of Thin Crystals* (Krieger, Florida, 1977)

[22] P. A. Midgley and M. Weyland, Ultramicroscopy **96** 413 (2003)

[23] J. W. Matthews, in *Epitaxial Growth, part B*, chapter 8 pp560-601 (Academic Press, New York, 1975)

[24] W. M. Stobbs, in *Electron Microscopy in Materials Science: Proc. 3rd Int. School Electron Microscopy,* edited by U. Valdre and E. Ruedl Vol1&2 pp591-645 (1975)

[25] J. P. Hirth and J Lothe, *Theory of Dislocations* (Wiley, New York, 1982)

[26] J. W. Steeds, *Anisotropic Elastic Theory of Dislocations* (Clarendon Press, Oxford, U.K, 1973)

[27] O. Madelung, *Semiconductors-Basic Data*, 2nd ed (Springer, Berlin, Germany, 1996)

[28] S. Srinivasan, L. Geng, F. A. Ponce, Y. Narukawa and S. Tanaka, Appl. Phys. Lett. **83** (23) 5187 (2003)

[29] K. Maeda, M. Sato, A. Kubo and S. Takeuchi, J. Appl. Phys. **54** 161 (1983)

[30] L. Houben, M. Luysberg and T. Brammer, Phys. Rev. B **70** 165313 (2004)

[31] K. Maeda, K. Suzuki, Y. Yamashita and Y. Mera, J. Phys: Cond. Matt. **12** 10079 (2000)

[32] M. Jiang, Digital Image Processing. Available on-line at: http://iria.math.pku.edu.cn/~jiangm/courses/dip/html/node97.html (accessed September 2005)

Figure captions

Figure 1:

(a) Dark-field images recorded using the (0002) and (b) (11-20) reflections reveal that the Burgers vector of the majority of dislocations (>90%) have an **a**-component and 50% of the total have a **c**-component. Line-vectors for the threading dislocations are parallel to the <0001> zone axis.

Figure 2:

Bands of dislocation half-loops are seen in plan-view bright-field images of the annealed p-GaN films. Delaminating cracks appear towards the right of the dislocation loops. Similar dislocation bands were also seen in non-RTA treated films.

Figure 3:

Dark-field images of dislocation loops observed at the edge of the crack (lower right, black contrast) taken with (a) the (01-10) reflection, (b) the (-1010) reflection and (c) the (1-100) reflection. All the bowed dislocation loops have identical Burgers vector: **b**=[11-20]/3. Several in-plane dislocations are seen extending from the crack for about 1μm when imaged in the (1-100) reflection.

Figure 4:

Dark-field LACBED patterns of the crack-tip observed in the {11-20}-reflection (a). Prior to the crack-tip, little lattice twist is seen across the dislocation bundles, whilst some bending of the rocking-curve indicates thin-film buckling (b). The rocking-curve shears abruptly across the crack body, indicating a large twist in the lattice either side (c). Large rotations of the rocking curve (~50mrad) are correlated with the high density of dislocation loops seen in figure 3 at the sides of the crack body (c), indicating a dislocation spacing of ~60Å.

Figure 5:

The area used for WBDF tomography seen at a crystal tilt of -60^{o} in its original (a) and filtered forms (b). Each dislocation type stands out well; threading dislocations appear vertical and in-plane dislocations extend across the field of view. Dislocation

bundles associated with a crack-tip (**C**) are observed, while threading edge-dislocations (**A**) form domain boundaries.

Figure 6:

The tomographic reconstruction of the same area as seen in figure 5. Threading dislocations (**A**) associated with low-angle domains are reproduced, as are the in-plane dislocations (**B**). These are in fact threading dislocation that turn over close to the crack (**C**) and glide away to become in-plane screws (**D1, D2** and **D3**). One of these (**D2**) interacts directly with a threading dislocation (**D**), whilst another (**D3**) appears to change habit plane briefly (**E**). An in-plane dislocation (**F**) glides into this area from an adjacent area and terminates at the upper surface. The intensity of the 'dust' is stronger at the specimen edge (**G**) and relates to the strong thickness fringes seen in figure 5. The boxes delineate the sub-volumes that are re-projected to give the cross-sectional views of the in-plane dislocations shown in figure 8.

Figure 7:

Detailed views of a sub-volume taken from figure 6 that contain the in-plane dislocations. The viewing angles correspond to (a) 45^{o} and (b) 70^{o} specimen tilts and show that threading dislocations turn over within the bundle (**C**) to become in-plane screws (**B**). The height at which the dislocations (**D1-3**) turn over is seen to vary, suggesting no common slip plane between them. The interaction between the threading and basal-plane segment (**D**) is verified.

Figure 8:

In-plane projections of the dislocation reconstructed within the two boxes of figure 6. The three dislocations labelled **D** are reconstructed with high definition with a 2:1 aspect ratio along the c-axis (upwards in this diagram). The in-gliding dislocation, labelled **F**, is reconstructed as a broad arc.

Figure 9:

A simple test-object comprised of 3 dislocations (a) used to demonstrate the depth resolving ability of stereographic reconstruction (b) and tomographic reconstruction (c) of in-plane dislocations. The stereographic error is about 20nm, whereas the tomographic resolution is better than 5nm.

Figure 10:

A schematic diagram of the reconstruction (dashed circle) of a basal-plane screw dislocation (black dot), viewed along its line vector, with images obtained for the full 360^{o} tilt range (a). Several WBDF peaks are shown for different imaging directions with the dotted line indicating the back-projected view from each of these. In an isotropic material, the reconstruction is a circle (b). For an anisotropic material (with $c_{66}>c_{44}$), the full reconstruction is an ellipse (c). Images taken over a limited tilt range results in an arc (solid line). When the tilt-axis and diffracted beam directions do not coincide exactly, the arc becomes asymmetric along the **c**-axis, as indicated (d).

Figure 11:

Schematic diagram of the plastic relaxation of post RTA, Mg-doped GaN. A bundle of dislocation loops extend for several tens of microns along the <1-100> directions (**1**) before reaching the delaminating crack (**2**). At the sides of the crack, <11-20> dislocation loops (**3**) of identical Burgers vector are seen to extend outwards. Threading dislocations (not shown) pervade the region with line vectors pointing along the **c**-axis, i.e. out of the plane of the paper. During the RTA anneal, threading dislocations in the vicinity of the crack turn over and glide along the <2-1-10> directions, leaving basal-plane screw segments (**4**). The diagram is not to scale.

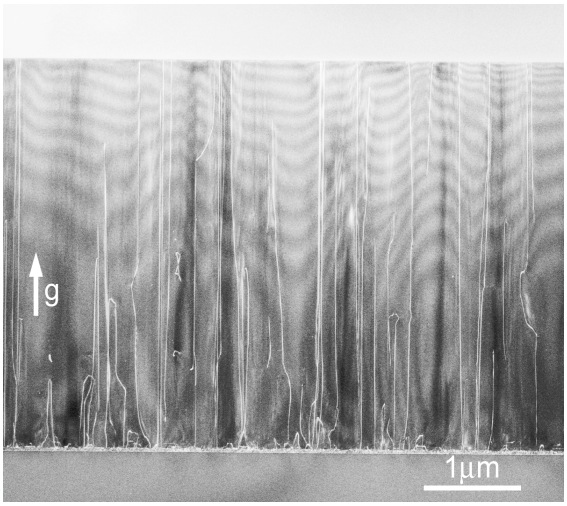

(a)

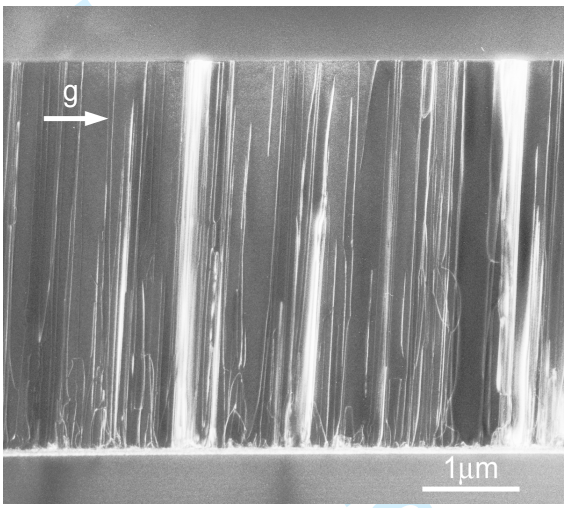

(b)

Figure 1.

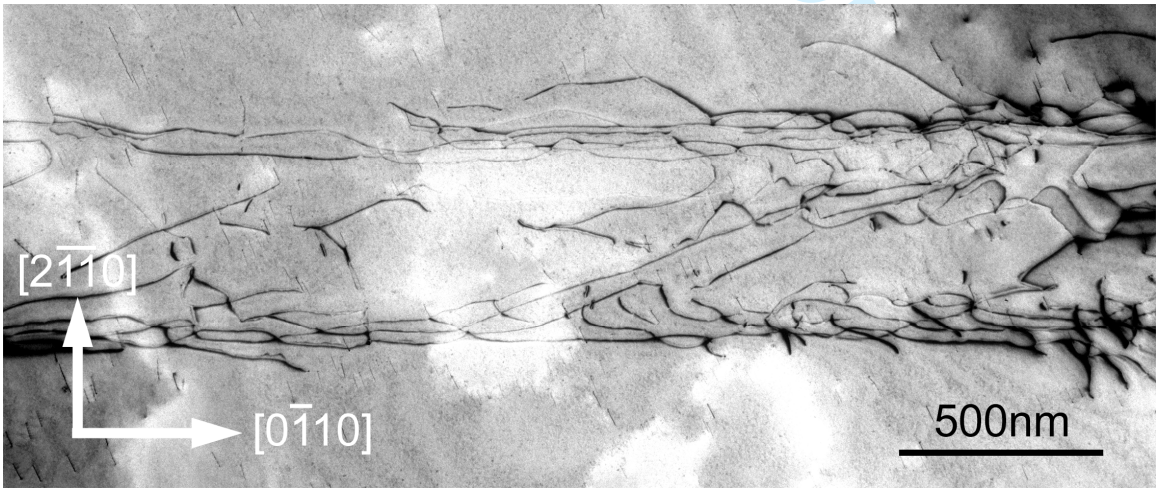

Figure 2.

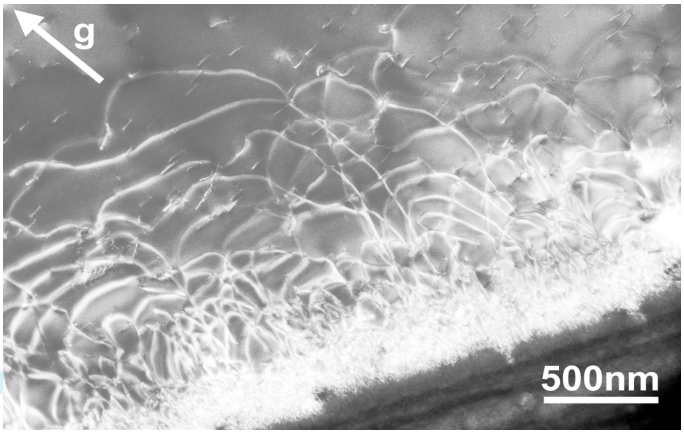

(a)

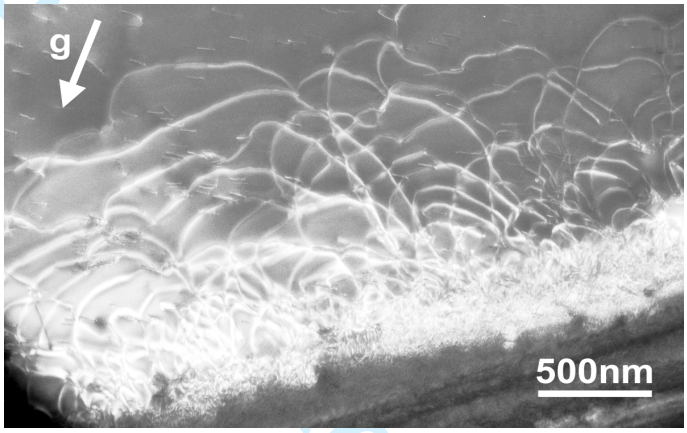

(b)

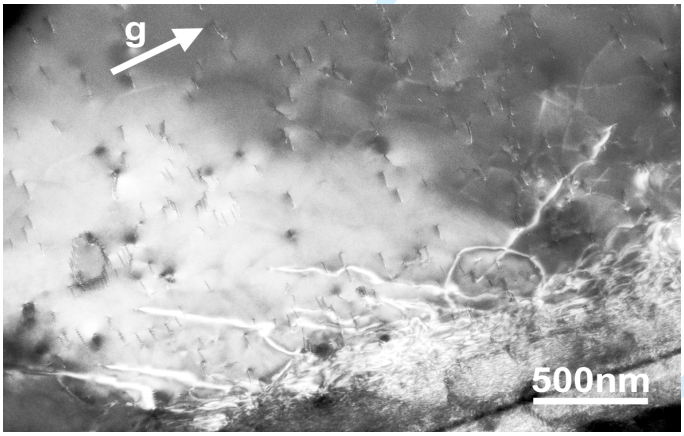

(c)

Figure 3.

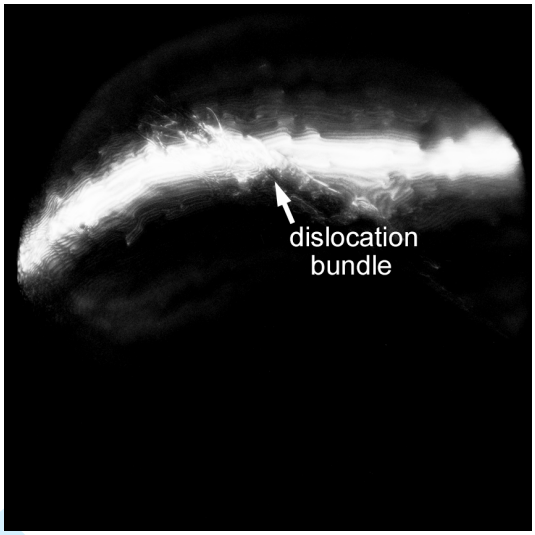
dislocation
bundle

(a)

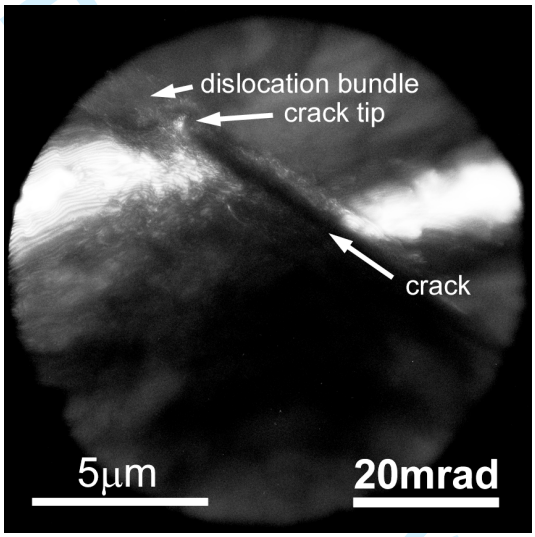
dislocation bundle
crack tip
crack
5μm
20mrad

(b)

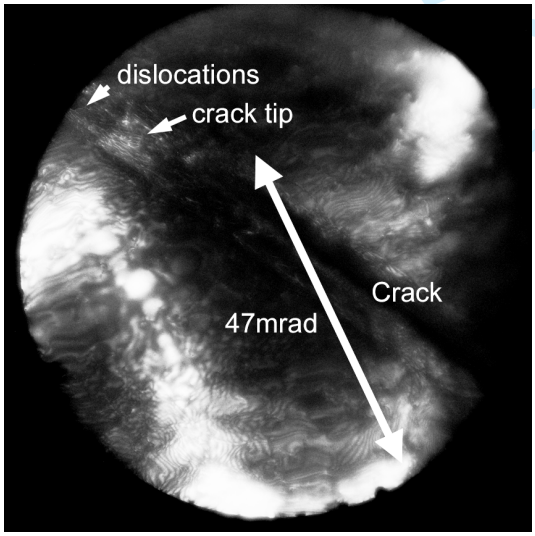
dislocations
crack tip
Crack
47mrad

(c)

Figure 4.

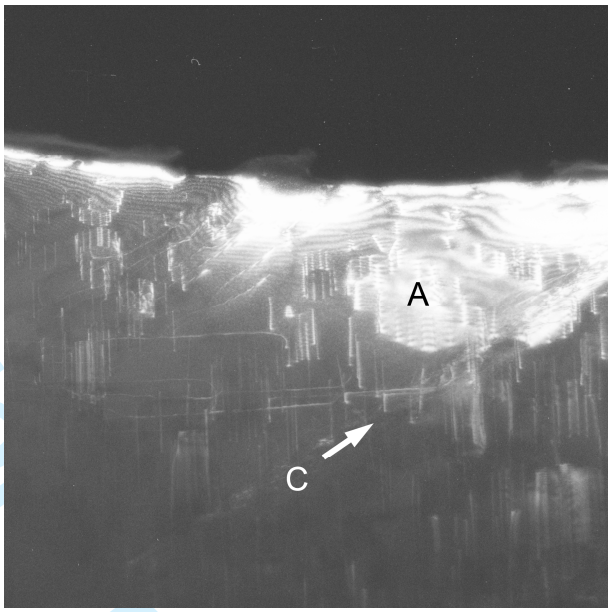

(a)

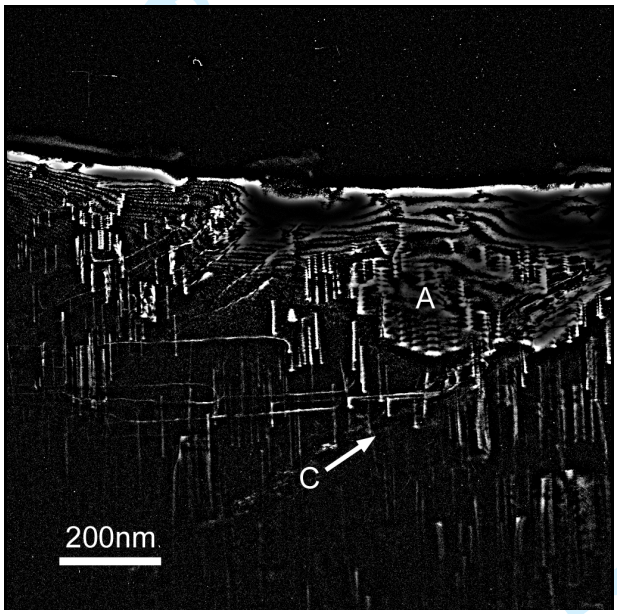

(b)

Figure 5.

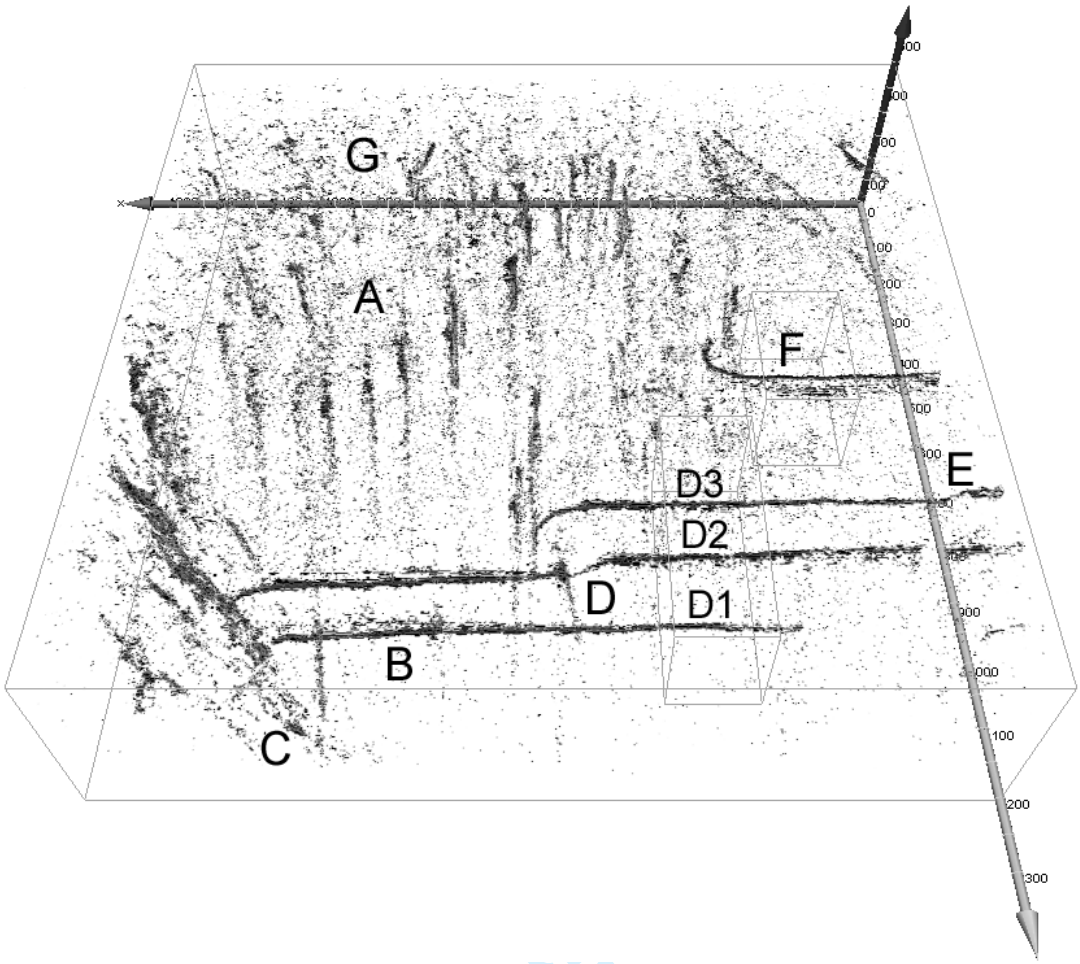

Figure 6.

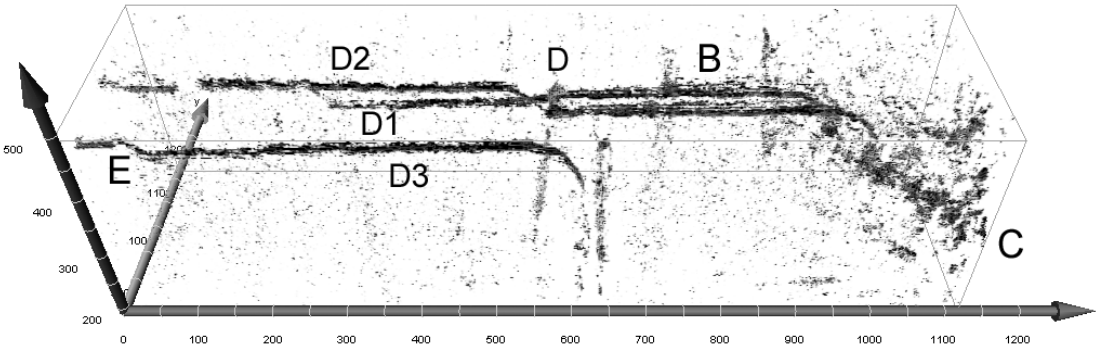

(a)

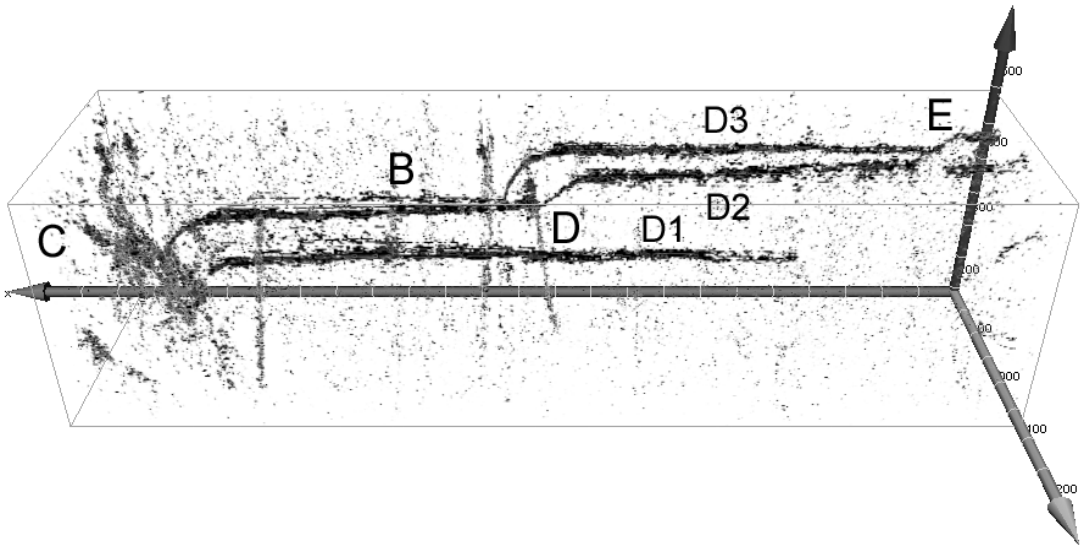

(b)

Figure 7.

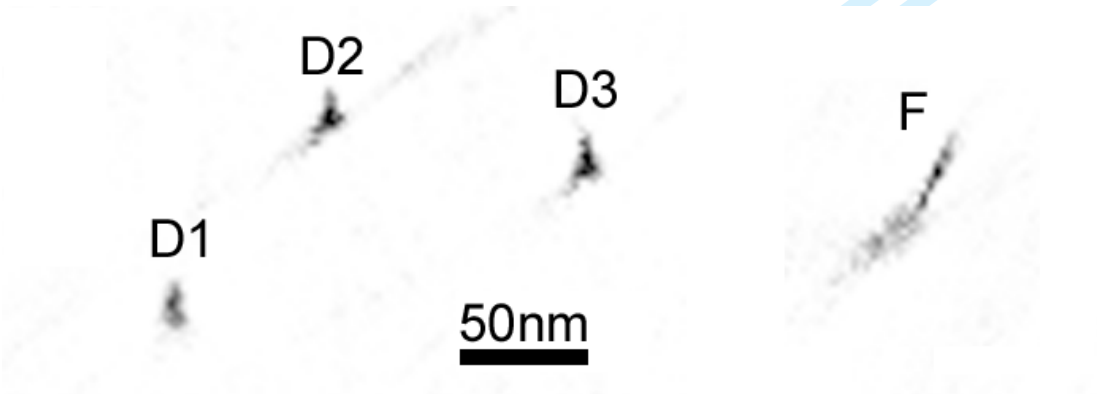

Figure 8

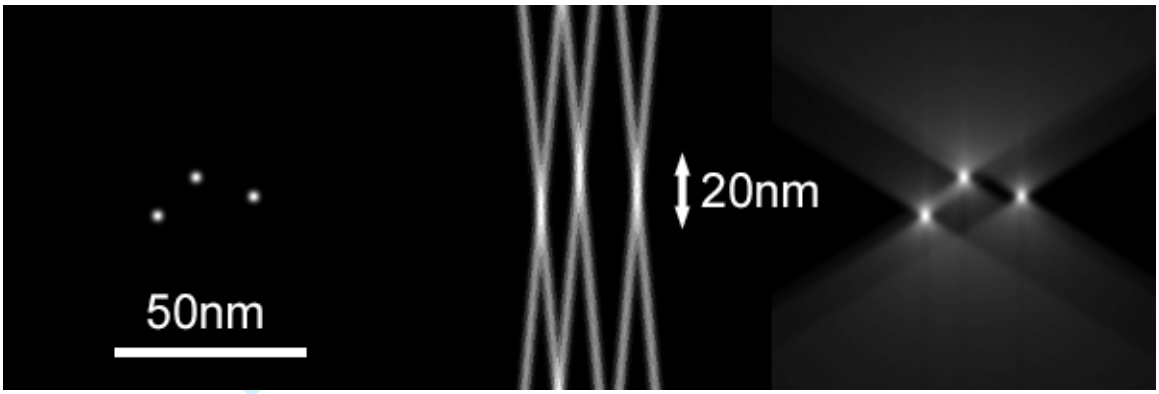

(a) (b) (c)

Figure 9

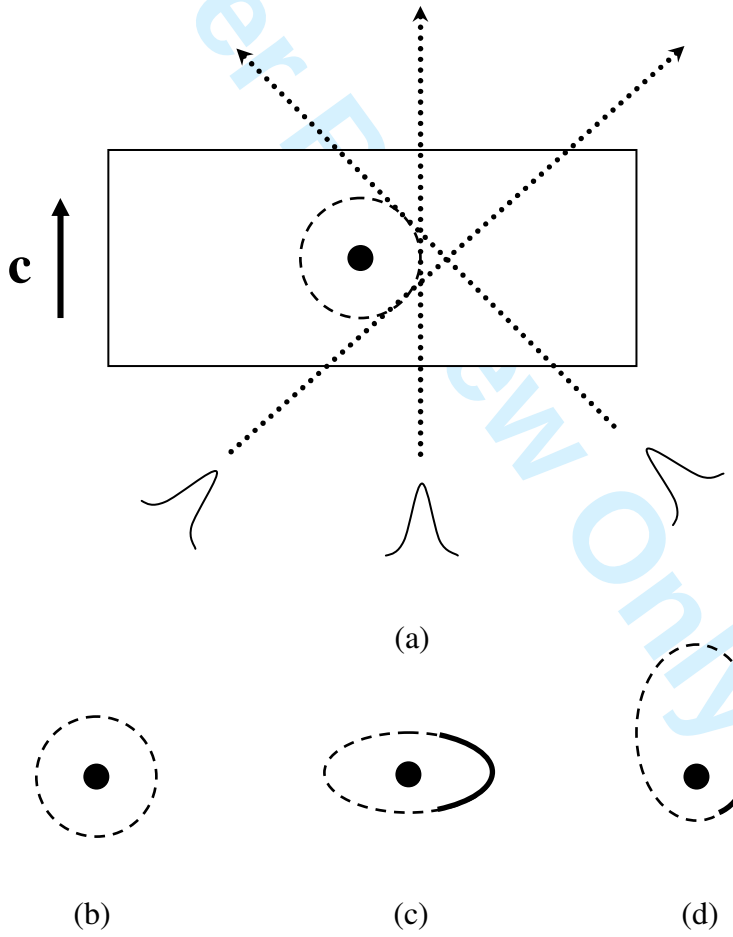

(a)

(b) (c) (d)

Figure 10

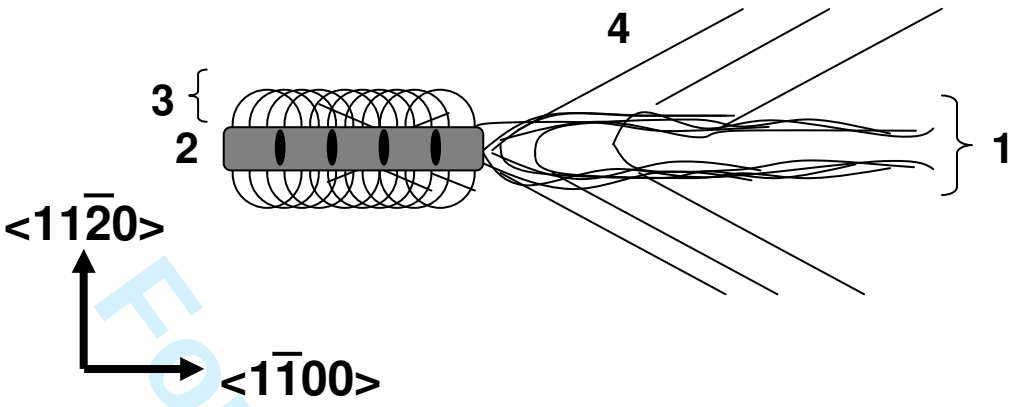

Figure 11